Pattern formation on ion-irradiated Si surface at energies where sputtering is negligible

A. Lopez-Cazalilla,[1,*] D. Chowdhury,[2] A. Ilinov,[1] S. Mondal,[2,3] P. Barman,[2,4] S. R. Bhattacharyya,[2] D. Ghose,[2] F. Djurabekova,[1,5] K. Nordlund,[1] and S. Norris[6]

[1]*Department of Physics, P. O. Box 43, FIN-00014 University of Helsinki, Finland*
[2]*Saha Institute of Nuclear Physics, Sector – I, Block – AF, Bidhan Nagar, Kolkata 700064, India*
[3]*Maharaja Manindra Chandra College, 20 Ramkanto Bose Street, Kolkata 700003, India*
[4]*Homi Bhaba National Institute, Training School Complex, Anushakti Nagar, Mumbai 400094, India*
[5]*Helsinki Institute of Physics*
[6]*Department of Mathematics, Southern Methodist University, Dallas, Texas 75205, USA*

(Dated: June 1, 2018)

The effect of low energy irradiation, where the sputtering is imperceptible, has not been deeply studied in the pattern formation. In this work, we want to address this question by analyzing the nanoscale topography formation on Si surface, which is irradiated at room temperature by Ar^+ ions near the displacement threshold energy, for incidence angles ranging from 0 to 85°. The transition from smooth to ripple patterned surface, i.e. the stability/instability bifurcation angle is observed at 55°, whereas the ripples with their wave-vector is parallel to the ion beam projection in the angular window of 60-70°, and with 90° rotation with respect to the ion beam projection at the grazing angles of incidence. A similar irradiation setup has been simulated by means of molecular dynamics, which made it possible, firstly, to quantify the effect of the irradiation in terms of erosion and redistribution using sequential irradiation and, secondly, to evaluate the ripple wavelength using the crater function formalism. The ripple formation results can be solely attributed to the mass redistribution based mechanism, as erosion due to ion sputtering near or above the threshold energy is practically negligible.

I. INTRODUCTION

Ion irradiation of solids is well-known as a one-step technique to induce a variety of periodic nanostructures like ripples, nanodots, and holes on a wide range of substrates - without any mask or photoresist - by only varying different process parameters[1,2]. This technique has already been studied for many years[3–6]. The advantages of the ion beam nanopatterning method increase the curiosity to understand the fundamentals behind the pattern formation, which is still not completely clear. The most widely adopted theory to explain the ion beam induced pattern formation phenomena was proposed by Bradley and Harper (BH theory) in 1988[7]. In this work, a surface instability during ion irradiation is considered to arise due to the effect of competition between surface curvature dependent ion erosion and smoothing via thermally induced surface diffusion. The theory successfully demonstrates evolution of the ripple pattern and its orientation with respect to the ion beam projection due to oblique incidence ion beam sputtering (IBS). Additionally, experimental observations of e.g. orthogonal rotation of ripples after a certain grazing incidence or exponential growth of a ripple amplitude for initial sputtering time can be successfully explained by the BH theory. However, one of the predictions of this theory, namely the evolution of surface instability/ripples at all oblique incidences, does not match with most of the reported experimental results of surface stability/smoothening at near-normal incidence angles $\theta \leq 45°$[8]. This shortcoming has been addressed by Carter and Vishnyakov (CV), who considered the effect of atoms displaced by the collision cascade, but remaining on the surface[9]. Modeling these atoms as a surface flux in the direction of the projected ion beam, they obtained a curvature-dependent smoothing term whose wave number dependence exactly matches those of the roughening term in the BH theory, but is stabilizing rather than destabilizing, and therefore predicts a smooth surface at near-normal incidences. Surprisingly, it was later concluded both experimentally[10] and via simulations[11] that at least for energies less than 1 keV, mass redistribution appears to be a dominant mechanism at most ion incidence angles, causing not only smooth surfaces near normal incidence, but also the "parallel-mode" ripples that emerge around 45°. However, erosion seems to remain critical to the subsequent ripple rotation observed near grazing incidence[12].

In this work, we investigate the role of mass redistribution of surface adatoms in the pattern formation process during ion irradiation experimentally as well as theoretically for the whole range of angles θ from 0°-85° with respect to the surface normal. For this purpose, we choose the projectile energy to be close to or below the displacement threshold energy in Si (E_d are 35 eV for Frenkel pair formation and 23 eV for bond defect formation[13], respectively). Such ultra-low energy ions, when incident on a solid, come to rest within the first few atomic layers on the target surface by losing their kinetic energy through single knock-on collisions with the atoms of the target. Consequently, the target atoms are displaced with the energy below the surface binding energy (∼5 eV[14]), not having enough energy to leave the system, and thus, mostly remain on the surface in form of adatoms or

their higher-order clusters[15,16]. Recently, Norris et al.[11] explained pattern formation as a function of an incident angle using the crater function formalism, and showed that the mass redistribution in surface dominates the formation of nanoscale topographies during ion impacts of energies <250 eV. On the other hand, experimentally the pattern formation with such ultra low energy inert gas ion irradiation was previously observed on insulator surfaces, e.g., on mica[17] at room temperature and on semiconductor surfaces, e.g., Ge[18] and GaAs[19] surfaces near their re-crystallization temperatures, respectively.

In order to understand better the effect observed in the experiments, we introduce a computational model that represents a sequential irradiation of a localized surface region. By focusing the impact region to a certain area of the cell, it is possible to speed up the process of formation of a structure that can be studied precisely using molecular dynamics (MD) methods. The accumulated damage eventually results in a significant structure modification. We decompose the observed effect into cumulative atomic redistribution and the erosion components, demonstrating the significance of redistribution especially for the lower ion energies.

II. METHODS

A. Experimental procedure

The commercially available mirror polished p-type Si (100) single crystal wafers of approximate size 1 cm × 1 cm were used in the experiments. Before ion irradiation, the samples were cleaned with acetone followed by methanol in an ultrasonic bath for 10 min each. The samples were irradiated by 30 eV Ar^+ ions for ion incidence angles 0° to 85° with respect to surface normal in a high vacuum sputtering chamber with a residual pressure of 10^{-8} mbar. A broad ion beam of diameter 3 cm was extracted from an inductively coupled RF discharge ion source equipped with three graphite grid ion optical system (M/s Roth & Rau Microsystems GmbH, Germany)[18]. A plasma bridge neutralizer was used for charge neutralization of the sample as well as of the sputtering chamber. During irradiation, the chamber base pressure was $\sim 10^{-4}$ mbar, the ion current density was about 52 μ A.cm^{-2}. Also, during the irradiation, the ion fluence was kept fixed at 1×10^{19} cm^{-2} for all incidence angles. The ion fluence (1×10^{19} cm^{-2}) has been calculated by following the relation $t = De/J\cos(\theta)$ where t is the sputtering time, D is the fluence, e is the charge of electron (1.6×10^{-19} C), J is the ion current density and θ is the incidence angle. D and J are fixed for all ion incidence angles. To keep the ion fluence fixed, the irradiation time has been varied corresponding to $\cos(\theta)$ of each incidence angle. The irradiated samples were characterized by atomic force microscope operating in the tapping mode with tip radius 10 nm using a Nanoscope IV multimode SPM. All the AFM images were analyzed by using the Nanotec Electronica SL WSxM software (version 5.0)[20].

B. Computational model

All the simulations in the study were performed by using the PARCAS MD code[21,22], which allows for collection of information about different components, which may contribute to surface pattern formation, such as sputtering, atomic displacements and internal stress.

The potential used in the simulations for the Si-Si interaction was the environment-dependent inter-atomic potential (EDIP)[23,24], complemented by the purely repulsive ZBL potential at short distances[25]. The Ar-Si interaction was described by the pure repulsive ZBL potential[26]. The Ar-Ar interaction were described using the pair potential with high energy repulsive part from DFT DMol calculations[25] joined smoothly at small distances to the LJ equilibrium part[27]. This combination has already been tested in the previous work and demonstrated a reasonable representation of Si and a-Si properties under high energy impacts[28].

In all simulations presented in this work, we used the simulation cell, which was cut out from the larger amorphous Si cell, which was previously carefully relaxed in Ref. 28. The size of the cell was selected to be sufficient to enclose fully the collision cascades developed during the simulations of low energy ion impacts. Prior to the irradiation simulations, the cell was equilibrated at 300 K as follows: the initial cell periodic in all three directions at 0 K was thermalized to 300 K using the Berendsen thermostat[29] during 100 ps. After that, the pressure was relaxed in the NPT ensemble by using the Berendsen algorithm[29] during the following 50 ps, at the temperature 300 K. Finally, a 1 nm thick layer at the bottom was fixed (immobilized) in order to prevent system motion during the sequential irradiation, the surface was opened and the structure was relaxed during 100 ps. The final size of the cell was 16.56 x 16.56 x 5.15 nm^3, which was composed of 73584 atoms (density 0.05212 nm^{-3}) and periodic boundary conditions were applied in x and y directions. The radial distribution function (RDF) is demonstrated in Fig. 1 and compared with experiments[30,31]. Although the agreement with experiments is not perfect, also the experimental curves show some variation. This is likely because differently synthesized pieces of amorphous Si have slightly different atomic scale structure[32].

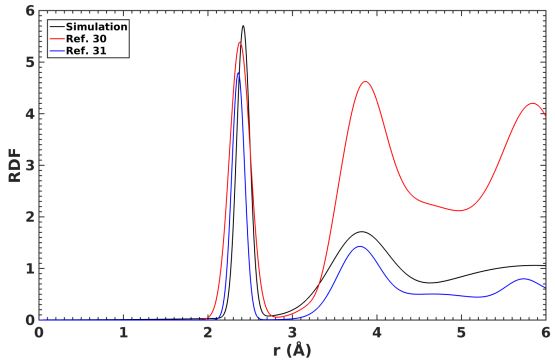

FIG. 1: RDF for: Si atoms in the initial a-Si cell at 300 K (black), for Ref. 30 (red) and for Ref. 31 (blue).

In the following, we describe two kinds of simulations: sequential ion impacts (every following ion was impacting on the surface which has been affected by the previous ion impacts) and individual ion impacts (every new ion entered a pristine surface) carried out in order to analyse the mechanisms of the pattern formation by low energy irradiation.

1. *Sequential irradiation*

Irradiation simulations of the sequential impacts were carried out as follows. Every ion entered the surface in the middle of the simulation cell. We randomized the position of the entrance in the Y direction by randomly shifting the cell over periodic boundary prior to every subsequent irradiation event. The X coordinate was selected randomly only within a small interval of the length 1.62 nm, corresponding to 10% of the total cell length in the X direction. This way we can focus the effect induced by incoming ions within a small region. This model is beneficial from an MD method point of view, since in such a planar focused mode of the ion beam (see Fig. 2), we need to simulate fewer ion impacts to reach the same local fluences as those reached in the experiments with regular broad beams before the ripples of appreciable size become apparent[33,34]. Moreover, in the selected scenario we will be able to verify whether ultra-low energy ions induce cumulatively sufficient relocation of surface atoms to render visible modifications of surface morphology, since they can be observed within the MD time span. Mainly we present the results obtained with the 30 eV Ar ions to match the experimental condition. The incident angles in our simulations ranged from 55° to 85° including with intermediate steps of 65°, 70°, 80°. For completeness of the analysis, we also ran the simulations with the 20 eV and 250 eV Ar ions under the 70° of incidence.

In the irradiation simulations, a thermal bath region with 0.8 nm thickness was applied during the first 21 ps after each ion impact event, and, subsequently, the entire cell was cooled down to 300 K during 10 ps time prior to a next irradiation to maintain the desired conditions. During the simulations, we removed those atoms which penetrated through the fixed layer. Sputtered atoms were also removed at the end of every ion impact event.

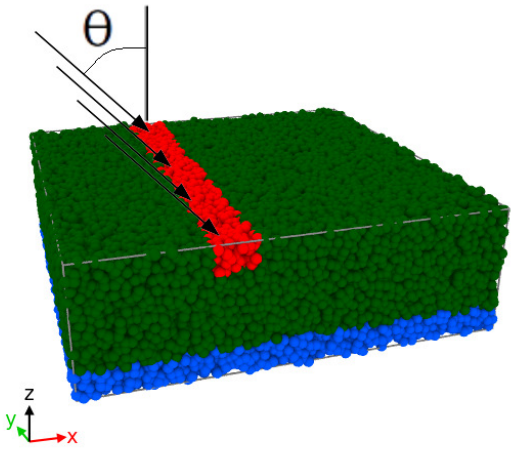

FIG. 2: Simulation cell. Red color demonstrates the irradiation region. Blue atoms form a fixed layer.

In this type of simulations, we cannot apply the same crater function formalism as in Ref. 11, 28, and 35 to analyze the results obtained in the sequential ion impact simulations. Since the total displacement is a cumulative quantity it may depend on the curvature of the surface, which is gradually changing in these simulations during the bombardment as a function of ion fluence and energy of incoming ions.

Instead of using the crater function formalism, to quantify our analysis we estimate the effect of the displacement by measuring the x and z components of the total displacement (sum of the displacement vectors of all atoms). It has been demonstrated before[11,28] that, due to symmetry, the mean value of the component perpendicular to the projection of the ion beam on the surface (y component) is approaching zero as the number of events increases. Therefore, we estimated the total displacement as

$$\begin{aligned} \delta_x &= \sum_{i=1}^{N_{displaced}} (x^i_{final} - x^i_{initial}) \\ \delta_z &= \sum_{i=1}^{N_{displaced}} (z^i_{final} - z^i_{initial}) \end{aligned} \tag{1}$$

where δ_x and δ_z are the components parallel with the projection of the ion beam on the surface and normal to the surface, respectively. These allow us to construct the overall magnitude of the displacement vector via

$$\delta_{xz} = \sqrt{\delta_x^2 + \delta_z^2}. \tag{2}$$

2. Individual irradiation events

Ion beam induced pattern formation phenomena as a function of the ion incidence angle is generally explained by the BH theory[7] based on the curvature dependent sputtering process. The advantage of using the crater function theory over the BH theory is that it includes both the sputtering and redistribution effects and has been refined by many authors recently[35–38]. During irradiation, energetic ions create surface vacancies as target atoms are sputtered out or dislodged from its original positions, which leads to the formation of the crater holes. On the other hand, the dislodged atoms which are not able to leave the surface, i.e. adatoms generate the crater rim. The first-order moments (M_x or M_y) of the crater function give the redistribution of mass where the zeroeth-order moment M_0 determines the sputtering yield. The role of the displaced and sputtered atoms as well as their combined effect on the evolution of surface height during ion irradiation is given by the following continuum equation:

$$\frac{\partial h}{\partial t} = \Gamma_x(\theta)\frac{\partial^2 h}{\partial x^2} + \Gamma_y(\theta)\frac{\partial^2 h}{\partial y^2} - K\nabla^4 h \qquad (3)$$

where, K is a coefficient of surface energy relaxation by a mechanism such as surface diffusion or thin-film viscous flow, and $\Gamma_x(\theta)$, $\Gamma_y(\theta)$ describe the effect of sputter erosion and mass redistribution. These coefficients are defined via[11,39]

$$\begin{aligned}\Gamma_x(\theta) &= \frac{\partial}{\partial\theta}\left[I_0\cos(\theta)\,M_x^{(1)}\right] + \frac{\partial}{\partial K_{11}}\left[I_0\cos(\theta)\,M^{(0)}\right]\\ \Gamma_y(\theta) &= \left[I_0\cos(\theta)\cot(\theta)\,M_x^{(1)}\right] + \frac{\partial}{\partial K_{22}}\left[I_0\cos(\theta)\,M^{(0)}\right]\end{aligned} \qquad (4)$$

(At the low energies considered here, because erosion is negligible, we expect $M^{(0)} \approx 0$, and so only the first terms in each definition are nonzero.) When $\Gamma_x(\theta) < 0$, one expects the formation of the parallel mode ripples, whereas $\Gamma_y(\theta) < 0$ corresponds to the perpendicular mode ripples, respectively. The moment $M_x^{(1)}$ describes the net change in the location of mass on the surface. Lateral mass redistribution, which moves mass forward from the impact point, makes a positive contribution to this quantity, while erosion, which sputters atoms ahead of the impact point, makes a negative contribution. As ion incidence angle increases, the redistributed mass is extended further from the point of impact along the downstream direction which causes an increase in the moments, until a critical angle at which ion reflection begins to reduce the overall momentum transfer. Previously, the angle dependent first order moment $M_x^{(1)}$ for 100 and 250 eV Ar^+ and Si combination was calculated by Norris et al.[11] using MD simulations.

In order to extract the crater function moments[35] needed to determine the probable formation of ripples at the studied low energies, we performed also the simulations of individual impact events. In these simulations, we utilized the same single ion irradiation setup as in earlier publications[11,28], but the a-Si target used in the simulations is the same as described in Sec. II B. For simulations of individual irradiation events, the system was relaxed to 0 K in order to minimize the background displacements for better accuracy in extraction of the atomic displacements, following the methodology used in Ref. 28.

In the simulations, a 30 eV Ar ion positioned at 1 nm above the surface was always directed towards the center of a-Si cell. The simulation time is 30 ps during which the Berendsen thermostat[29] with the time constant of 50 fs is applied to a 0.8nm thick region along the borders of the cell in the x and y directions. The initial cell is shifted along the periodic directions randomly so every irradiation is performed in a different atomic environment of the amorphous structure in order to obtain a statistically significant result; azimuthal angles are selected randomly.

The irradiation angles θ are selected to be 0°, 15°, 30°, 45°, 60°, 70°, 80°, 85° and 87° off-normal; 200 independent irradiation simulations have been performed with each angle.

III. RESULTS & DISCUSSION

A. Experimental results

AFM images of Fig. 3 illustrate topographical evolution of 30 eV ion irradiated Si surfaces at room temperature and for ion incidence angles θ ranging from 0° to 85° with respect to the surface normal. The irradiated surfaces do not show any distinct morphology for incidence angles up to 50°. Only, a few isolated dots are found randomly on surfaces. A weak ripple topography is found to appear at $\theta = 55°$, which can be considered as the threshold angle for the ripple formation for the present experimental conditions. The wave-vector of these ripples is aligned parallel to the ion beam projection. This can also be confirmed by the corresponding FFT image as the centre bright spot is found to elongate parallel to the projected ion beam direction. These kinds of ripples are well-known as parallel mode ripples. As the ion incidence angle increases to 65-70°, ripples become pronounced, regular and ordered which can also be easily realizable from the corresponding FFT images, where two well-separated symmetric lobes (1st order) around the centre spot in parallel direction of ion beam projection can be observed. The occurrence of the 1st order bright spot in FFT image signifies enhancement in the ripple ordering. Further increase of θ to 75°, results in disintegration of the parallel mode ripples and subsequent development of conical protrusions tilted along the ion beam direction. As a consequence, fourfold symmetric spot appears in the corresponding FFT image. The increase of higher incidence angle (80°) shows more tilted conical protrusions, but their height shows a steep fall. The increase in tilting can be confirmed from the FFT

image as the central spot shows elongation perpendicular to ion beam direction. Finally, at $\theta = 85°$, almost flat surface whose topographies are not clearly discernible from the AFM image (in real space) is again observed. However, its corresponding FFT image (in reciprocal space) shows more pronounced elongation of the central spot perpendicular to the ion beam projection. This clearly indicates the appearance of a surface topography with the wave vector perpendicular to the incident beam direction.

The ion incident angle dependent overall topographic evolution is quantitatively summarized in Table 1. The surface roughness ω remains constant up to 45° and starts to increase above 50° due to the evolution of surface topographies, i.e. due to appearing of the parallel mode ripples from 55° onwards. The maximum increase of roughness is observed at 75° and at further grazing incidences, ω again decreases. This variation is also depicted in Fig. 4. On the other hand, the wavelength of the parallel mode ripples is estimated from the 1st order peak position of the corresponding PSD curves, extracted from the corresponding FFT images (not shown here) are found to be around 35.3±1.5 nm.

We conclude with a comment on the perpendicular-mode structures seen at 80 and 85°. The only physical mechanism that readily predicts the formation of structures in this orientation is sputter erosion[7]. In contrast, neither mass redistribution [9,11,40] nor plastic flow due to stress injection[41,42] has been shown to predict anything but parallel-mode patterns. Therefore, the emergence of perpendicular-mode structures despite the lack of any significant erosion is quite interesting. The AFM images at 80° could be understood to show an underlying parallel-mode instability, upon which cones have grown later through some nonlinear process. However, the structures at 85°, while of small amplitude, are undeniably of purely perpendicular-mode orientation. This suggests interesting questions for future study.

TABLE I: Incidence angle dependent rms roughness, ripple wavelength and pattern orientation for 30 eV Ar^+ ion irradiation on Si(100) surface.

Ion energy (eV)	Angle (°)	Roughness (nm)	Wavelength (nm)	Mode
30	0	0.19±0.03		
	15	0.25±0.02		
	25	0.35±0.06		
	35	0.26±0.06		
	45	0.43±0.15		
	55	0.59±0.04		parallel
	60	0.79±0.07		parallel
	65	1.17±0.16	35.3±1.5	parallel
	70	1.45±0.09	40.9±1.1	parallel
	75	6.93±0.15		mixed
	80	1.16±0.09		perpendicular
	85	0.42±0.03		perpendicular

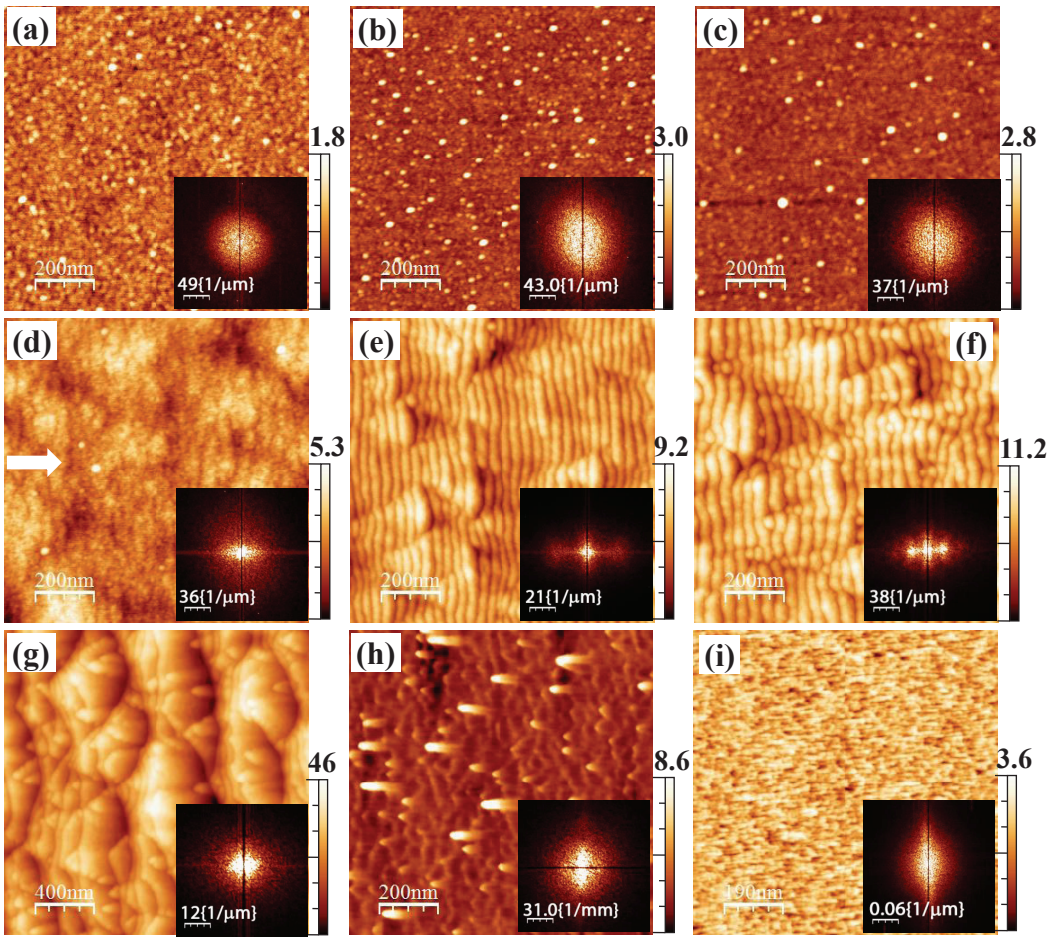

FIG. 3: Representative AFM images of the evolution of morphology at different ion incidence angles: (a) 0°, (b) 25°, (c) 35°, (d) 55°, (e) 65°, (f) 70°, (g) 75°, (h) 80° and (i) 85° for Ar^+ ion irradiation of energy 30 eV, current density 52 μA cm^{-2} and fluence 1 $\times 10^{19}$ ions cm^{-2}. The inset shows the corresponding FFT images and the white arrow indicates the beam direction for oblique incidence ion irradiation.

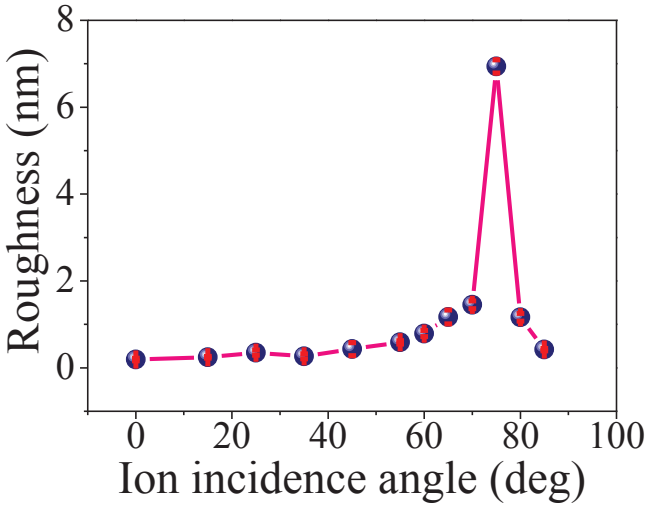

FIG. 4: RMS roughness variation of Si surface topographies as a function of the ion incident angle. Si surface was bombarded by 30 eV Ar^+ ions at room temperature and at fluence 1×10^{19} ions cm^{-2}.

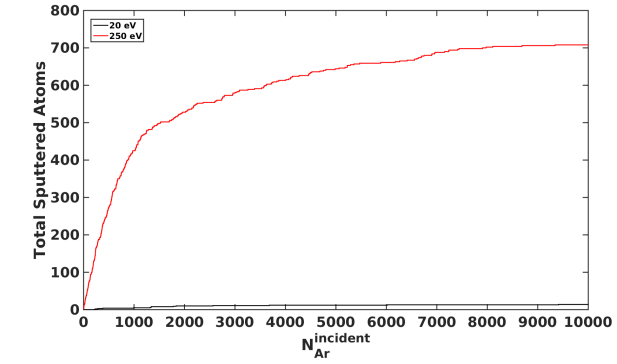

(a)

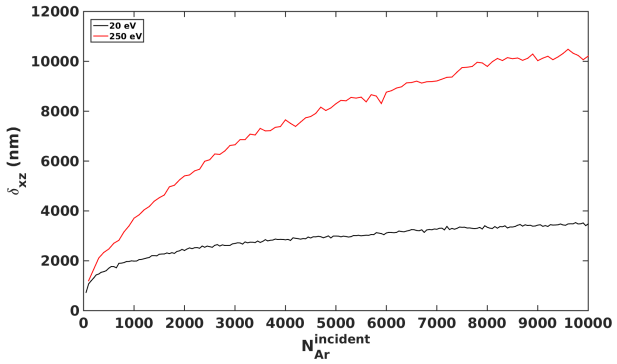

(b)

FIG. 5: (a) Total number of sputtered atoms (N_{sputt}) and (b) total atomic displacement obtained (δ_{xz}) at $\theta = 70°$ of incidence as a function of the number of incoming Ar ions.

B. Simulation results

1. *Sequential irradiation*

In order to understand the energy margins for any modification of the surface morphology, we first present a comparative study of two cases of the sequential irradiation with the energy of 250 eV that is rather low, but still much higher than the displacement threshold in Si and may result in sputtering, and with the energy of 20 eV, which is well below the displacement threshold (≈ 35 eV). Of course, the surface atoms have lower threshold values[43], but overall, this comparison may give a good idea of whether sputtering plays a crucial role in the pattern formation, since the Ar ions with the energy of 20 eV will not be able to cause any significant sputtering.

In Fig. 5, we plot the total displacement calculated according to Eq. 2 as a function of the number of incoming ions.

As expected, we observe much stronger sputtering by the 250 eV ions than by the 20 eV ones; in addition, the cumulative number of the sputtered atoms grows faster with the number of incoming ions in case of the 250 eV ions (see Fig. 5a). Moreover, the number of atoms sputtered by the 20 eV is barely visible on the linear scale of the graph in Fig. 5a, and it remains negligible through the whole sequential run at this ultra low energy. This result may indicate that the visible surface pattern formation can be expected only for the higher energy, if erosion is the dominating factor.

The total atomic displacement with respect to the initial structure, in turn (see Fig. 5b) increases progressively for both energies, 20 eV and 250 eV, during the sequential irradiation process. This indicates that although the structure is relaxed during 10 ps after every ion impact event (see Section II B 1), the effect of individual ions does not disappear completely. On the contrary, the system remains partially strained, which provides a contribution to the total deformation of the structure during the following impact. Since the displacements are accumulated gradually, this process may lead to the changes in surface morphology, forming ripples. We note also that the total atomic displacement is accumulated faster for

the ions with the 250 eV energy.

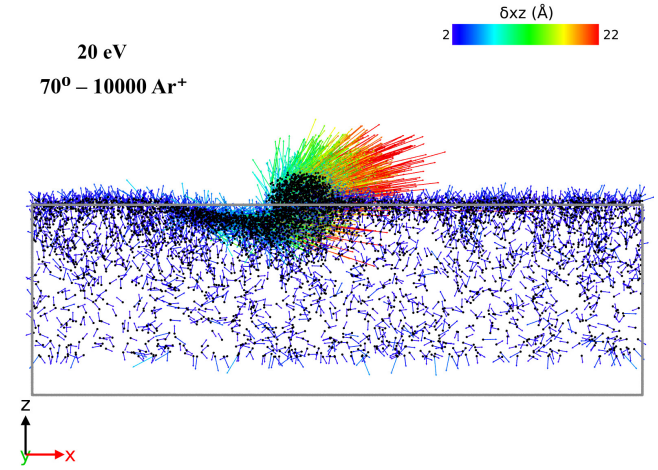

(a)

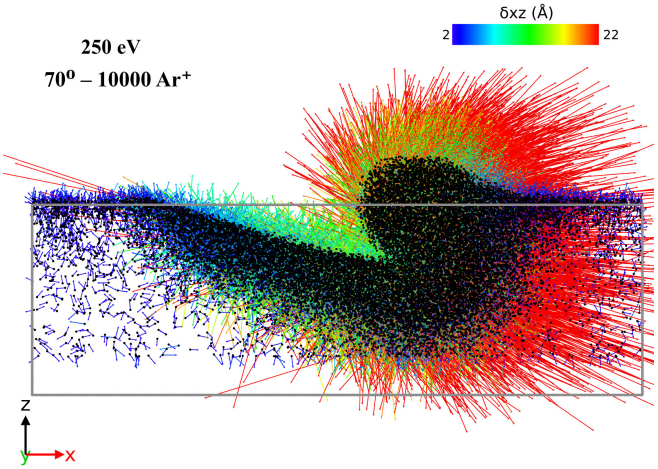

(b)

FIG. 6: Final structure after 10000 consecutive impacts of Ar ions on a-Si target at 70° off-normal for (a) 20 eV, (b) 250 eV ion energies. Displacement vectors are shifted for clarity and colored according to their magnitude.

Despite the stronger sputtering for the ions 250 eV and almost no sputtering for the ions of 20 eV, we observe the formation of similar ridges on the surface during the simulations performed for the ions with the indicated energies impacting on the surface at 70° off-normal, which are shown in Fig. 6. Here we show atoms which were found after the full sequential run of 10000 ions with the corresponding energy, to be displaced for more than 2 Å (black dots) and their displacement vectors, sized and colored according to the displacement magnitude. Displacement vectors (the vectors which are connecting the initial and final positions of the same atom) are translated along their directions in such a way that the beginning of the vector is at the initial position of its end, in other words, at the displaced position of the atom. This is done for the clarity of visualization, and the initial positions of the atoms can be easily restored by translating the vectors back to the original position.

Comparing the features created by the same amount of the 20 eV and 250 eV Ar ions in a-Si, respectively (see Fig. 6), we can clearly see that the size of the ridges is different, while the shape of these features are quite similar. The 250 eV Ar ions sputter more Si atoms, and the erosion is much stronger during the first stages of the irradiation, which creates a deeper groove. The following incoming ions push the material in the positive x direction, as the displacement vectors show in Fig. 6b. On the other hand, in the 20 eV case, the erosion is almost negligible. If so, we were not expecting formation of a groove, while Fig. 6a shows the formation of a similar ridge, which we see for the 250 eV Ar ions. We attribute the formation of the groove purely to the redistribution effect, as the displacement vectors show (see Fig. 6a) the momentum transferred in the focused beam mode is accumulated in smaller displacements, but eventually relaxed towards the open surface rather than inwards the surface as in case of the 250 eV ions. The momentum transferred to the atoms in the collisions creates a local stress, which provokes the material flow towards the surface.

A more detailed analysis we perform for the ions of the 30 eV energy to match the experiment. In Fig. 7, we show how the shape of the groove formed in the planarly focused ion beam depends of the atomic displacement effect caused by the incoming ions as a function of the incident angles. We selected a few representatives angles, 55°, 65°, 70°, 80° and 85° off-normal. In these figures, we depict atoms and their corresponding displacement vectors for all atoms with the displacements not shorter than 2 Å similarly as in Fig. 6. In these simulations we again did not observed any significant sputtering effect. From the left to the right panel of Fig. 7, we show the evolution of the ridge formed by the ions incoming at the same incident angle (2000 ions on the left and 10000 ions on the right). We see that for all cases, the groove is growing with the number of incoming ions, however, the size is overall reducing with increase of the incident angle and at the angle greater than 80°, the surface remains practically intact even after long sequential irradiation.

In the following, we present a quantitative analysis of the results obtained in our MD simulations of the sequential irradiation process.

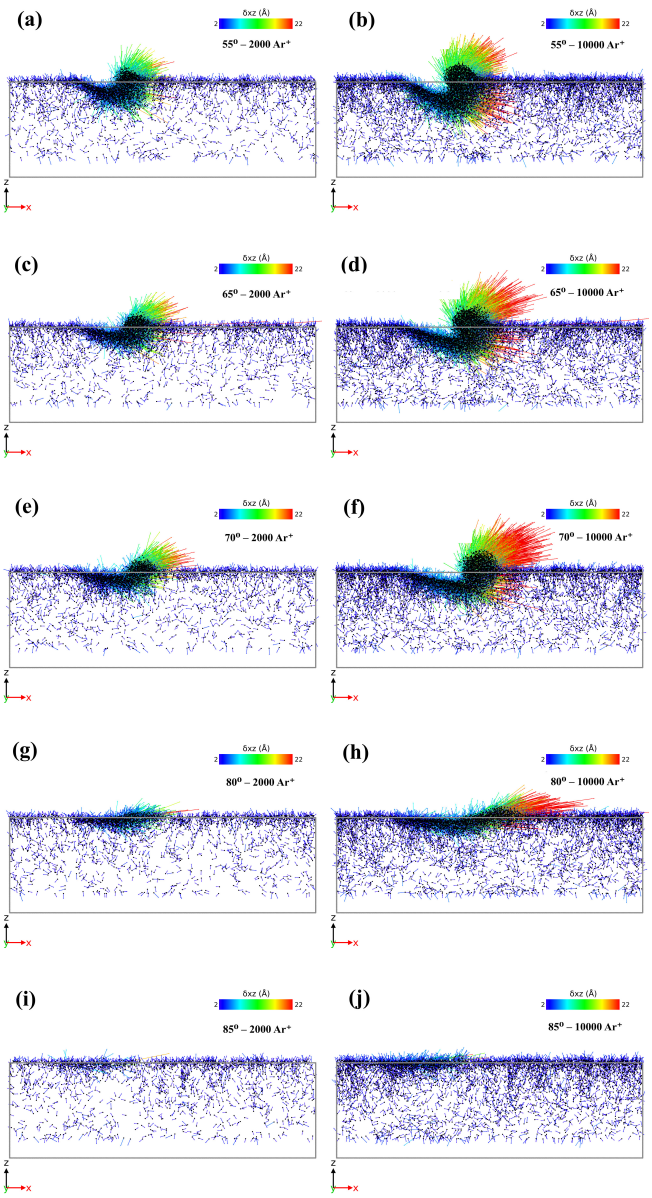

FIG. 7: Atoms (black dots) and their displacement vectors after the sequential irradiation of a-Si by 30 eV Ar ions obtained with different incident angles: $\theta = 55°$ (a, b); $\theta = 65°$ (c, d); $\theta = 70°$ (e),(f); $\theta = 80°$ (g, h); $\theta = 85°$ (i, j); and two fluences 2000 ions (a, c, e, g, i) and 10000 ions (b, d, f, h, j). Displacement vectors are shifted for clarity and colored according to their magnitude (as in Fig. 6)

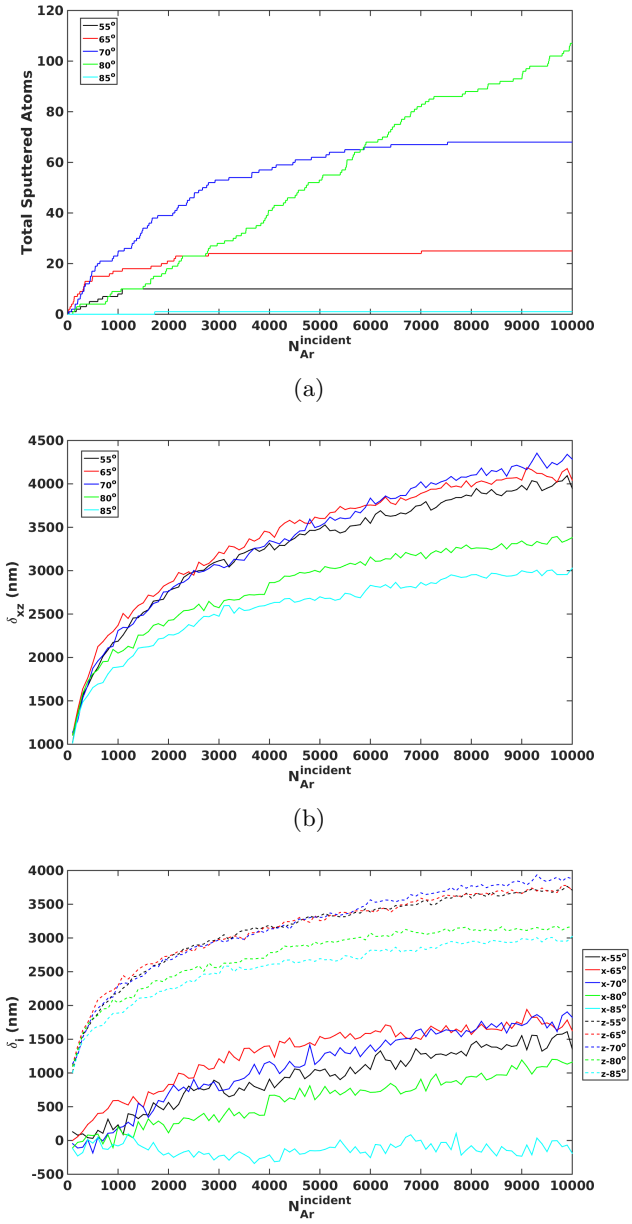

(a)

(b)

(c)

FIG. 8: (a) Total number of sputtered atoms (N_{sputt}), (b) total atomic displacement and (c) x and z components of the total atomic displacement as functions of incoming ions.

Fig. 8a shows that the maximum erosion effect in the target is caused by the 80° sequential irradiation, and it is the only case in which the total number of sputtered atoms is continuously growing, while in other cases it reaches the saturation level, indicating that no more sputtering takes place after a certain fluence. We looked closer in the simulation details to understand the reason of this saturation. At a certain point, depending on the irradiation angle, a ridge formed on the surface by the atomic redistribution becomes sufficiently large to

capture sputtered atoms which redeposit on the ridge increasing its size. However, in the 80° case, the change in the surface morphology is not so marked, the shadowing effect is smaller and the sputtering continues also after 10000 impacts.

We also analyze the dependence of the total accumulated displacement on the incident angle. In Fig. 8b, we observe that the ions incoming at 70° of the incidence induce larger total displacement than at any other studied angles. This result agrees well with the experiments, which show a maximum effect at about 70° (see Fig. 4). For 55 and 65°, the observed total displacements are only slightly smaller than those of the 70° case. The largest difference we observe for the closest to grazing incidence, which resulted in much smaller total displacement. This result is in line with the fact that the shape transformation on the surface is less pronounced (Fig. 7h) for the 80° incidence, although the number of sputtered atoms in these simulations is the highest. In the case of 85°, we cannot observe any visible ridge formation effect during the simulation.

In Fig. 8c, we can clearly see how the angle θ affects the contribution to the x and z displacement components. In all cases, the z component dominates the value of the total displacement, mainly due to the relaxation time after every impact and the effect of the open surface in z direction; the contribution of the x component decreases with θ angles approaching the grazing incidence, which results in a smaller ridge formation on the surface. On the other hand, at the 55°, 65° and 70° incident angles, the formation of a ridge on the surface is more pronounced. In the case of the grazing incidence of (85°), the x contribution oscillates around zero during the entire process, which shows that the displacement accumulation in direction parallel to the ion beam is almost negligible due to the generated recoils. The recoils are displaced equally along and opposite to the positive x direction.

As we reported in Fig. 8a, the erosion in the surface caused by ions of 30 eV at any angle of incidence is extremely low. Even after 10000 Ar^+ ion impacts, in the most extreme case, the total number of sputtered particles is 110, which corresponds to an average sputtering yield of 0.011. Based on our analysis, we conclude that the momentum transferred from low energy ions incoming under a tilted incidence is insufficient to cause erosion of the material, the process which is commonly used to explain the nanopatterning formation on amorphous surfaces. Instead we see that this momentum causes significant redistribution of surface atoms, which is becoming a crucial factor leading to formation of a groove on the surface. Moreover, those rare atoms which receive sufficient momentum to be sputtered, are captured by the groove, contributing to its further growth.

2. *Single ion irradiation*

In this section, we present the results extracted from our MD simulations, using the mathematical model developed by Norris et al.[35] and applied similarly as in the previous works on this topic[11,28]. Using the zeroeth, first erosive and redistributive crater function moments it is possible to estimate $\Gamma_{x,y}$ and determine when it becomes negative (unstable regime) so ripples can be observed. Specially, this model is useful for analysis whether this is an effect of the erosion or, on the other hand, redistribution.

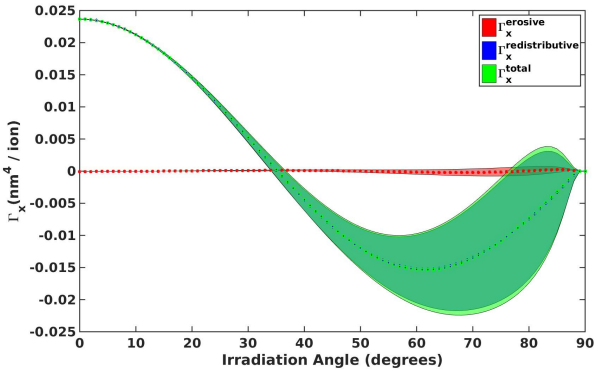

(a)

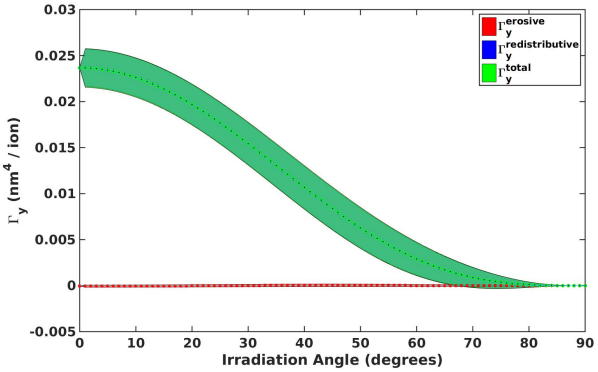

(b)

FIG. 9: Results for singe 30 eV Ar^+ on a-Si. (a) Coefficient $\Gamma_x(\theta)$. (b) Coefficient $\Gamma_y(\theta)$. Shaded regions represented one σ confidence interval (68.2 %), dotted lines represent the mean.

The results in the Fig. 9 show the coefficient estimation considering the error bars from the calculated crater function moments. It is evident that redistribution is dominating the value of the coefficients in both cases because the zeroeth and the first erosive moments are much lower compared to the first redistributive. Considering that, according to the prediction, ripple formation can be observed starting from $\theta = 35°$. The parallel mode (Γ_x) is dominating in the unstable regime, but as we can see from the Fig. 9b within the error bars, the Γ_y co-

efficient becomes negative, which is consistent with the perpendicular to the ion beam pattern prediction. However, the probability of the perpendicular mode ripples being formed is very small.

The ripple wavelength is estimated using the following expression[11,28]

$$\lambda(\theta) = 2\pi\sqrt{\frac{2B(\theta)}{-f\Gamma_{x,y}(\theta)}}, \tag{5}$$

where f is the ion beam flux, $B(\theta)$ is the viscous flow coefficient. The criteria used to choose either the parallel (to the ion beam projection) (Γ_x) or the perpendicular coefficient (Γ_y), is the most negative (unstable) one. In case of both coefficients being non-negative, a surface instability will not appear.

The value of the flux $f = 3.25 \times 10^{14}\text{cm}^{-2}\text{s}^{-1}$ is calculated according to the experimental fluence at $\theta = 0°$ and the corresponding exposure time. The value of $B(\theta)$ has been estimated following the supplementary material included in Ref. 11 by modifying the number of recoils generated per ion impact (using the Kinchin-Pease[44] model) but instead of considering a constant value for the amorphous layer thickness, we calculate it as twice the penetration depth[45]. The penetration depth is calculated for the simulated irradiation angles using MDRANGE code[46]. The calculated ripple wavelength is presented in Fig. 10.

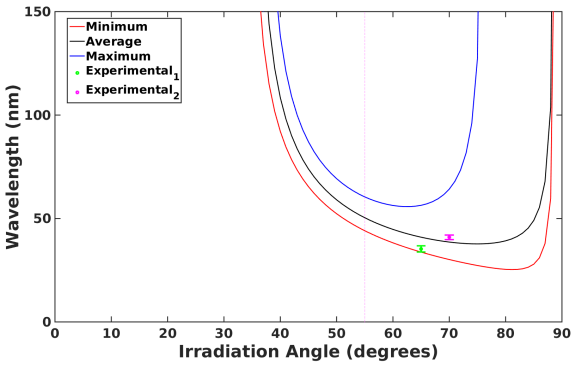

FIG. 10: Wavelength prediction for single 30 eV Ar^+ on a-Si, after applying a flux of $f = 3.25 \times 10^{14}\text{cm}^{-2}\text{s}^{-1}$ using the mean, the lower and the upper error boundary estimations for Γ_x and Γ_y coefficients shown in Fig. 9. The magenta vertical dotted line indicates the experimental critical angle. The green and pink dots represent the experimental point measured in this work for 65° and 70° respectively.

According to the results in the wavelength estimation we can see that the instability prediction starts from 35°, while the experimental critical angle has been observed at around 55°, showing that the model is not taking into consideration possible additional effects that experimentally contributes to the stability at middle irradiation angles. On the other hand, the experimental wavelength values are accurately predicted as they fall between the lower and the upper boundary estimations.

IV. CONCLUSIONS

In summary, the effect of the low energy 30 eV Ar^+ ion irradiation on Si surface is investigated both experimentally and by MD simulations at different incidence angles. The transition from a flat surface to the parallel mode ripples is observed experimentally at 55°, whereas parallel to perpendicular mode transition occurs at 75°.

The sequential focused irradiation simulations performed in order to understand the reasons of the pattern formation at low irradiation energies confirm that the sputtering is almost negligible for 30 eV Ar on a-Si. Hence, the formation of the ridge structure is a pure effect of atomic redistribution. Besides, the larger the total displacement is, the faster the growth of the ridge.

The single ion irradiation results, which are analysed in the crater function formalism, also show that sputtering does not affect the pattern formation in this case, because the contribution of the redistributive part is much stronger. The dependence of the viscous flow coefficient on the irradiation angle proves to be an important factor in the wavelength estimation, as the thickness of the amorphous layer stimulated by ion impacts depends on this angle. This model is able to predict the ripple wavelength quantitatively well as a product of the redistribution mainly, even though the transition to the perpendicular mode ripples is not predicted at the grazing incidence. Though Γ_y coefficient lower boundary is negative for irradiation angles larger than 68°, the probability of the perpendicular mode ripples appearing is very small, due to the lower boundary of Γ_x coefficient is larger in magnitude than the corresponding boundary Γ_y coefficient in the instability region.

ACKOWLEDGEMENTS

The ion irradiation of the Si and the characterization of irradiated samples were done with the facilities at Saha Institute of Nuclear Physics (SINP), Kolkata, India. DC, SM, PB, SRB and DG want to acknowledge the Director, SINP for his kind support in this work.

The computational work was performed within the Finnish Centre of Excellence in Computational Molecular Science (CMS), financed by The Academy of Finland and University of Helsinki. Computational resources provided by CSC, the Finnish IT Center for Science as well as the Finnish Grid and Cloud Infrastructure (persistent identifier urn:nbn:fi:research-infras-2016072533) are gratefully acknowledged.

* Corresponding author alvaro.lopezcazalilla@helsinki.fi

[1] W. L. Chan and E. Chason, J. Appl. Phys. **121301**, 46 (2007).

[2] J. Muñoz-García, L. Vázquez, R. Cuerno, J. Sánchez-García, M. Castro, and R. Gago, edited by Z. M. Wang, Springer, Dordrecht **10**, 323 (2009).

[3] S. Facsko, T. Dekorsy, C. Koerdt, C. Trappe, H. Kurz, A. Vogt, and H. Hartnagel, Science **285**, 1551–1553 (1999).

[4] U. Valbusa, C. Boragno, and F. Buatier de Mongeot, J. Phys.: Condens. Matter **14**, 8153 (2002).

[5] A. e. a. Cuenat, Adv. Mater. **17**, 2845 (2005).

[6] B. Ziberi, F. Frost, T. Höche, and B. Rauschenbach, Phys. Rev. B **72**, 235310 (2005).

[7] R. M. Bradley and J. M. Harper, J. Vac. Sci. Technol. **6**, 2390–2395 (1988).

[8] D. Chowdhury and D. Ghose, Adv. Sci. Lett. **22**, 105 (2016).

[9] G. Carter and V. Vishnyakov, Phys. Rev. B **54**, 1764717653 (1996).

[10] C. S. Madi, E. Anzenberg, K. F. L. Jr., and M. J. Aziz, Phys. Rev. Let. **106**, 066101 (2011).

[11] S. A. Norris, J. Samela, C. S. Madi, M. P. Brenner, L. Bukonte, M. Backman, F. Djurabekova, K. Nordlund, and M. J. Aziz, Nature communications **2**, 276 (2011).

[12] W. Eckstein, R. Dohmen, A. Mutzke, and R. Schneider, Max-Planck Institute for Plasma Physics, IPP reports 12/3 (2007) and 12/8 (2011).

[13] E. Holmström, A. Kuronen, and K. Nordlund, Phys. Rev. B **78**, 045202 (2008).

[14] *CRC handbook of Chemistry and Physics*, 85th ed. (Taylor & Franciss, Boca Raton (FL), 2004-2005).

[15] T. Michely and C. Teichert, Phys. Rev. B **50**, 11156 (1994).

[16] F. Karetta and H. M. Urbassek, J. Appl. Phys. **71**, 5410 (1992).

[17] A. Metya and D. Ghose, Appl. Phys. Letters **103**, 161602 (2013).

[18] D. Chowdhury, D. Ghose, and S. A. Mollick, Vac. **107**, 23 (2014).

[19] D. Chowdhury, D. Ghose, S. A. Mollick, B. Satpati, and S. R. Bhattacharyya, Phys. Status Solidi B **252**, 811 (2015).

[20] H. R. Fernández, J. M. Gómez-Rodríguez, J. Colchero, J. Gómez-Herrero, and A. M. Baro, Rev. Sci. Instrum. **78**, 013705 (2007).

[21] M. Ghaly, K. Nordlund, and R. S. Averback, Phil. Mag. A **79**, 795 (1999).

[22] K. Nordlund, M. Ghaly, R. S. Averback, M. Caturla, T. D. de la Rubia, and J. Tarus, Phys. Rev. B **57**, 7556 (1998).

[23] M. Z. Bazant, E. Kaxiras, and J. F. Justo, Phys. Rev. B **56**, 8542 (1997).

[24] J. F. Justo, M. Z. Bazant, E. Kaxiras, V. V. Bulatov, and S. Yip, Phys. Rev. B **58**, 2539 (1998).

[25] K. Nordlund, N. Runeberg, and D. Sundholm, Nucl. Instr. Meth. Phys. Res. B **132**, 45 (1997).

[26] J. F. Ziegler, J. P. Biersack, and U. Littmark, (Pergamon, New York) (1985).

[27] C. Kittel, *Introduction to Solid State Physics*, 3rd ed. (John Wiley & Sons, New York, 1968).

[28] A. Lopez-Cazalilla, A. Ilinov, L. Bukonte, F. Djurabekova, K. Nordlund, S. Norris, and J. Perkinson, Nucl. Instr. Meth. Phys. Res. B **414**, 133 (2018).

[29] H. J. C. Berendsen, J. P. M. Postma, W. F. van Gunsteren, A. DiNola, and J. R. Haak, J. Chem. Phys. **81**, 3684 (1984).

[30] J. Fornter and J. S. Lannin, Phys. Rev. B **39**, 5527 (1989).

[31] K. Laaziri, S. Kycia, S. Roorda, M. Chicoine, J. L. Robertson, J. Wang, and S. C. Moss, Phys. Rev. Let. **82**, 3460 (1999).

[32] E. Holmström, B. Haberl, O. Pakarinen, K. Nordlund, F. Djurabekova, R. Arenal, J. S. Williams, J. E. Bradby, T. C. Petersen, and A. C. Y. Liu, J. Non-Cryst. Solids **438**, 26 (2016).

[33] P. Süle and K. H. Heinig, The Journal of Chemical Physics **131**, 204704 (2009).

[34] E. O. Yewande, R. Kree, and A. Hartmann, Phys. Rev. B **75**, 155325 (2007).

[35] S. A. Norris, M. P. Brenner, and M. J. Aziz, Journal of Physics-Condensed Matter **21**, 224017 (2009).

[36] N. Kalyanasundaram, M. Ghazisaeidi, J. B. Freund, and H. T. Johnson, Appl. Phys. Lett **92**, 131909 (2008).

[37] N. Kalyanasundaram, J. B. Freund, and H. T. Johnson, J. Phys. Condens. Matter **21**, 224018 (2009).

[38] M. Z. Hossain, K. Das, J. B. Freund, , and H. T. Johnson, Appl. Phys. Lett. **99**, 151913 (2011).

[39] M. Harrison and R. Bradley, Phys. Rev. B **89**, 245401 (2014).

[40] B. Davidovitch, M. J. Aziz, and M. P. Brenner, Phys. Rev. B **76**, 205420 (2007).

[41] M. Castro and R. Cuerno, Appl. Surf. Sci. **258**, 4171 (2012).

[42] S. A. Norris, Phys. Rev. B **86**, 235405 (2012).

[43] E. Holmström, L. Toikka, A. V. Krasheninnikov, and K. Nordlund, Phys. Rev. B. **82**, 045420 (2010).

[44] H. Gnaser, *Low-energy ion irradiation of solid surfaces: Springer tracts in modern physics*, 3rd ed., Vol. 146 (Springer,, New York, 1999).

[45] H. Hofsass, Appl. Phys. A **114**, 401 (2014).

[46] K. Nordlund, Comput. Mater. Sci. **3**, 448 (1995).